Chemical Engineering Journal 381 (2020) 122641

Contents lists available at ScienceDirect

Chemical Engineering Journal

journal homepage: www.elsevier.com/locate/cej

3D printing nanocomposite gel-based thick electrode enabling both high areal capacity and rate performance for lithium-ion battery

Chuang Sun[a], Shuiren Liu[a], Xinlei Shi[a], Chao Lai[d], Jiajie Liang[a,b,c,*], Yongsheng Chen[b]

[a] School of Materials Science and Engineering, National Institute for Advanced Materials Nankai University, Tianjin 300350, PR China
[b] Key Laboratory of Functional Polymer Materials of Ministry of Education, College of Chemistry, Nankai University, Tianjin 300350, PR China
[c] Tianjin Key Laboratory of Metal and Molecule-Based Material Chemistry and Collaborative Innovation Center of Chemical Science and Engineering (Tianjin), Nankai University, Tianjin 300350, PR China
[d] School of Chemistry and Materials Chemistry, Jiangsu Normal University, Xuzhou, Jiangsu 221116, PR China

HIGHLIGHTS

- 3D porous and highly conductive thick electrodes were designed by 3D printing.
- 3D-printed thick electrodes were constructed by using nanocomponents-based hybrid ink.
- 3D-printed electrodes show both high areal capacity and rate performance.
- This strategy represents a simple process for the preparation of thick electrodes.

GRAPHICAL ABSTRACT

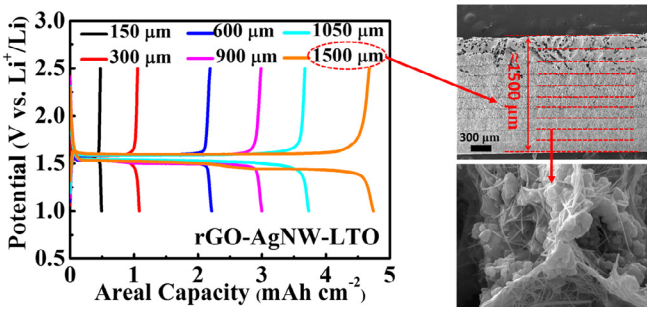

ARTICLE INFO

Keywords:
3D printing
Silver nanowire
Graphene
Lithium-ion battery
Thick electrode

ABSTRACT

The development of robust performing lithium-ion batteries (LIBs) with high areal capacity is a challenge that persists to date. One commonly used strategy to increase areal capacity is increasing the thickness of the battery electrodes. However, the practical application of these thick electrodes is hindered thanks to the fundamental issues of incomplete electrolyte infiltration, poor mechanical properties, and slow charge and ion transport. Herein, a new method is presented wherein a thick electrode is constructed by 3D printing a highly-conductive and hierarchical network of silver nanowires (AgNWs), graphene and $Li_4Ti_5O_{12}$ together as a mixed functional ink. The amalgamation of highly conductive AgNW network, interconnected 3D graphene scaffold, and hierarchical porous structure can allow the 3D-printed electrode to demonstrate much improved charge and ion transport, and to alleviate internal stresses during the charging and discharging process even under ultrahigh thickness state. As a result, the LIBs utilizing these thick electrodes have a rate capability of 121 mAh g^{-1} at 10C, high areal capacities up to 4.74 mAh cm^{-2}, and stable cycling performance (capacity retention of ~95.5% after 100 cycles). These performance metrics provide a route for a new design strategy using thick electrodes for high-performance energy storage devices.

* Corresponding author.
E-mail address: liang0909@nankai.edu.cn (J. Liang).

https://doi.org/10.1016/j.cej.2019.122641
Received 20 April 2019; Received in revised form 23 August 2019; Accepted 27 August 2019
Available online 28 August 2019

1. Introduction

Rechargeable lithium-ion batteries (LIBs) are ubiquitous in a plethora of industries and markets including electric vehicles, various consumer electronics, and the aerospace industry [1]. However, LIBs are intrinsically limited by the relatively low theoretical capacity of their active materials. When combined with the simplistic design of most batteries (i.e., electrode materials coated on metallic current collectors), existing LIBs in the marketplace have been unable to remain cost competitive and environmentally friendly [2,3]. Most attempts to mitigate these issues have targeted the former issue, with a multitude of studies on higher capacity materials published in recent years [4–7]. However, to date, there have been relatively few studies on the improvement of the design of the electrodes themselves [8–10]. Further work on this front is critical for the development of next-generation LIBs with higher areal capacity, faster charge–discharge rates, and enhanced lifetime.

One promising alternative approach is to utilize thicker electrodes (≫50 μm) to increase areal capacity [8–10]. Traditionally, scaling the thickness of the electrodes poses additional challenges including electrolyte infiltration, mechanical deformation, and reduced charge transport [11,12]. All else equal, the basic requirements for LIBs with thicker electrodes are to maintain baseline performance metrics for the aforementioned issues. As such, studies on thicker electrodes should focus on (i) development of strategies to control the electrode thickness [13]; (ii) maintaining high and continuous conductivity for fast charge transportation [9]; (iii) constructing a hierarchical porous structure to allow for complete electrolyte infiltration and effective ionic transfer [9,14]; and (iv) ensuring mechanical toughness to withstand internal stress fluctuations during charging and discharging [15]. In recent years, various reports have been published with this thick electrode design for high areal capacity LIBs [9,14,16]. Chen et al. demonstrated a thick electrode comprising a natural wood material as current collectors, followed sequentially by a slurry filling technique for high performance battery applications [9]. A recent report by Sander, et al. incorporated external magnetic fields and carbon templates in a thick electrode to enable fast charge transfer kinetics [14]. Wang et al. used electrospun titania-based fiber anodes in LIBs to achieve areal capacities up to 3.9 mAh cm^{-2} [16]. While these aforementioned works represent innovative designs for thicker electrodes, the complicated manufacturing necessitated and limited thickness control afforded hinders their adoption for commercial applications.

Extrusion-based three-dimentional (3D) printing is a potential avenue for electrode fabrication that is both low-cost and simple in terms of manufacturability. This technique is a layer-by-layer additive process with excellent control of thickness [17,18]. Typically, 3D-printed devices have relied on a single ink formulation, resulting in a relatively low rate performance for the resultant energy storage systems [19–21]. Though this technology is promising for the printing of thick electrodes, the viability of the ink thus poses yet another fundamental issues to overcome for the incorporation of thick electrodes.

Herein, we present the design and fabrication of a 3D porous and highly conductive thick electrode by 3D printing silver nanowires (AgNWs), graphene oxide (GO) and $Li_4Ti_5O_{12}$ (LTO) in a mixed functional ink (hereafter denoted as GO-AgNWs-LTO). This strategy represents a simple process for the preparation of thick electrodes through structure and material optimization. The well-distributed and highly conductive AgNW porous network facilitates the migration of electrons and ions to maintain high conductivity and the hierarchical porous structure allows complete electrolyte infiltration. Furthermore, the interconnected 3D graphene scaffold provides the mechanical strength required. Last, the LTO nanoparticles show low volumetric change upon cycling, which is yet another important criteria for the fabrication of thick electrodes [22]. The proposed design achieves the baseline criteria set previously, with the printed GO-AgNWs-LTO electrodes exhibiting an improved rate capability (discharge 121 mAh g^{-1} at 10C) and high-rate cycling performance (5C over 200 cycles). Other notable performance metrics include a thickness of ~1500 μm (with a high active material mass loading of ~30 mg cm^{-2}) and areal capacities of 4.74 mAh cm^{-2}. With regards to the stability of performance, it was observed that 1050 μm thick electrodes were able to maintain an areal capacity of 3.55 mAh cm^{-2} (with a capacity retention of ~95.5%) after 100 cycles at a current of 0.76 mA cm^{-2}. These areal capacities and cycling performance values are comparable to or surpass those of certain Si and metal oxide based devices, even though the gravimetric specific capacity of LTO is relatively lower [23–31]. These results indicate that the targeted thick electrode design offers a competitive strategy to achieve higher areal capacity, faster charge–discharge rates and more stable performance for batteries.

2. Experimental section

2.1. Raw materials

All chemicals used in this study were not further purified. AgNWs (1 wt% in water) were purchased from Zhejiang Kechuang Advanced Materials Co., Ltd. The average length and diameter of the AgNWs were 15–25 μm and 25–35 nm, respectively. GO with an average thickness of ~0.8 nm and a lateral size of ~1 μm was synthesized from spectral graphite by the modified Hummer method. LTO was acquired from BTR NanoTech Co., Shenzhen.

2.2. Preparation of 3D-printable inks

In a typical preparation, 2 mg mL^{-1} of the GO dispersion was prepared by dispersing GO in distilled water via sonication for 2 h, followed by adjusting the pH value to 6.5 by adding a 0.2 M NaOH aqueous solution. To prepare the GO-AgNWs-LTO ink, the LTO and GO solution were added into the aqueous AgNW solution (10 mg mL^{-1}) to a final wt. ratio of AgNWs:GO:LTO of 8:1:21. After sonication for 15 min, the mixture was vacuum filtrated using a PTFE membrane filter with a pore size of 0.45 μm, then washed with 100 mL of distilled water five times. The final ink had a mass ratio of AgNW:GO:LTO:water of 8:1:21:50. To prepare the GO-LTO ink, LTO was added into the GO dispersion to achieve a GO to LTO wt. ratio of 3:7. After sonication for 5 min, the GO and LTO mixture was vacuum filtrated using a PTFE membrane filter with a pore size of 0.45 μm. The final ink had a mass ratio of GO:LTO:water of 3:7:65.

2.3. Ink rheology

The rheological behavior of the formulated inks was probed using a DHR-2 rheometer (TA Instruments) with a 20 mm plate system and 1000 μm gap. All measurements were taken at room temperature (~25 °C). A preconditioning step at a shear rate of 0.1 s^{-1} for 10 s was applied before each test. A steady-state flow step test was performed to measure the shear viscosity of inks at shear rates from 0.1 s^{-1} to 1000 s^{-1}. PHS tests were performed at constant shear rates in three intervals (0.1 s^{-1} shear rate for 30 s, 200 s^{-1} for 30 s, and 0.1 s^{-1} for 100 s) to simulate the extrusion-based 3D printing progress. SSS tests were conducted at an oscillation stress of 1–1,000 Pa at a frequency of 1 Hz.

2.4. 3D printing electrodes

3D printing was done on a benchtop robot (FiSNAR F7304N) using a preprogrammed patterning procedure. The electrode framework with various layers (7 mm × 7 mm) was designed with a center-to center rod spacing of 500 μm and a rod diameter of 250 μm. Inks were stored in separate syringes for the printing process. The ink flow was controlled by an air-powered fluid dispenser (FiSNAR, DC100) with a nozzle pressure of 1.8 bar and a moving speed of 2 mm s^{-1}. After printing, the

electrodes were freeze-dried to remove the solvent, and subsequently treated with hydrazine hydrate vapor at 80 °C for 12 h to reduce the GO. Electronic Balance was used to measure the quality of electrodes directly. Mass loading of active materials were calculated by dividing the quality of active materials by area of electrodes.

2.5. Characterizations

SEM characterization was conducted using a field-emission SEM (JSM-7800) at an accelerating voltage of 5.0 kV. XRD analysis was performed using a powder X-ray diffraction system (Rigaku,TTR-III) equipped with Cu Kα radiation (λ = 0.15406 nm). The conductivity of was measured by Four-point probe measurements. Square Resistance of the single filament was measured with Four-point probe. Conductivity is the reciprocal of Square Resistance multiplied by filament thickness.

2.6. Electrochemical performance test

For the half cell test, rGO-AgNWs-LTO and rGO-LTO electrodes with various layers on copper were directly fabricated as the working electrode. Pure lithium foil was used as the counter electrode and reference electrode, Celgard 2300 used as the separator. 1 M $LiFP_6$ dissolved in a mixture of EC, DEC, and DMC with a volume ratio of 1:1:1 was used as the electrolyte. The cut-off potentials for charging and discharging were 2.5 and 1.0 V (vs. Li^+/Li), respectively. The galvanostatic charge/discharge measurement was conducted on a LAND-CT2001A battery test instrument (Wuhan, Jinnuo). The specific capacities are based on the LTO. CV measurements were taken at a scan rate of 0.5 mV s^{-1}. AC impedance measurements were taken in the frequency range of 10 mHz–100 kHz. These tests were carried out on a CHI 660E electrochemistry workstation from Shanghai Chenhua Instrument, Inc.

3. Results and discussion

A functional nanocomposite gel comprising 1D AgNWs, 2D GO nanosheets and 0D LTO nanoparticles was prepared according to our previously published method, with the performance heavily contingent on the intrinsic properties of its individual constituents [32–35]. AgNWs were selected as the base material for the ink due to its intrinsic electrical conductivity, compliant porous network structure, and ability to integrate with GO to form a viscous and thixotropic suspension without the use of additional polymeric thickeners [35]. As mentioned, GO nanosheets were utilized to aid in dispersing, thickening, and stabilizing to improve the printability of the electrode inks [35]. Furthermore, GO endows the system with mechanical toughness to stabilize the system during the volumetric expansion of the active material upon charging and discharging [35]. Last, LTO nanoparticles were utilized as the electrochemical active material due to the high theoretical capacity of LTO (175 mAh g^{-1}). In addition, LTO has been demonstrated to be a suitable alternative to conventional graphite due to safety concerns, fiscal benefits, and low volumetric change upon cycling [22].

A schematic illustration of the fabrication process for the 3D-printed inks is presented in Fig. 1a. This process can be broken down into three steps: (i) the fabrication of a well-dispersed and dilute mixture of LTO nanoparticles, AgNWs, and GO; (ii) the preparation of a hydrogel through vacuum-filtration of the diluted ternary suspension; and (iii) agitation of the hydrogel with a controlled volume of water for the gelation of the ternary nanocomponents. A chemical reduction process was also implemented to reduce the GO prior to conducting electrochemical performance tests. Electrodes are henceforth denoted as rGO-AgNWs-LTO and rGO-LTO, respectively, to denote the reduction of GO. As a note, because the system relies on water as the only solvent, this electrode preparation process is environmentally friendly.

The relative concentration of LTO:AgNWs:GO dictates the performance of the resultant ternary ink. In previous reports of 3D-printed electrochemical storage devices, GO-based inks have exhibited unique rheological properties when dispersed in high concentrations. As a result, pure GO-LTO ink is also discussed for comparative purposes in this manuscript, with the wt.% of LTO:GO at 7:3. In the ternary ink system, the optimal wt.% of the constituents were found to be 21:8:1 LTO:AgNWs:GO. To print the inks, the GO-AgNWs-LTO and GO-LTO inks were loaded into syringes with a 250 μm tip diameter and dispensed in a layer-by-layer arrangement on a copper disc by adjusting the compressed air pressure and printing rate. Due to the viscoelastic behavior of the inks, the individually dispensed lines can be stacked together to create complex mesh structures (7 mm × 7 mm). After the desired structure is printed, an overnight freeze drying process is employed to dry the electrodes. As an illustration, electrodes of different thicknesses are depicted in Fig. 1c. An expanded cross-sectional image is shown in Fig. 1d, where a ten layer ink is seen to have uniform thicknesses of ~150 μm per layer. This uniformity enables more uniform contact of adjacent filaments, and provides mechanical stability to the structure as a whole.

Because the performance of the 3D electrode is dependent largely on the structure of the ink, which in turn, is dependent on the rheological behavior of the ink, the rheological properties were investigated using a flat-plate rheometer [17,19–21]. The apparent viscosity of GO-AgNWs-LTO is shown in Fig. 2a, where the GO-LTO ink viscosities are observed to decrease linearly with increasing shear rates. This behavior is indicative of ideal shear-thinning thixotropic behavior of a non-Newtonian fluid, which enables the extrusion of the paste through a nozzle to form 3D patterns under moderate conditions. For the GO-LTO ink, this high viscosity is due to the high concentration (46 mg mL^{-1}) of GO. For GO-AgNWs-LTO inks (with a GO concentration ~20 mg mL^{-1}), the association of the nanocomponents within the ink leads to the ideal shear-thinning behavior. In this ternary system, the AgNWs generate a solid 3D network in the suspension [35]. The GO nanosheets, which contain hydrophilic oxygen-containing functional groups and hydrophobic polyaromatic graphene islands, serve as an associate thickener by winding and welding the AgNWs junctions to strengthen the connections [35]. The LTO nanoparticles occupy the voids between the 3D networks formed by the AgNWs and GO without impacting the interaction between the AgNWs and GO. Because of the synergistic reaction of all components, the same apparent viscosity can be realized in the ternary system, even at lower concentrations of GO.

Peak hold step (PHS) measurements were conducted to further quantify the rheological behavior. In these measurements, the ink was held at different shear rates for three different time intervals to simulate the actual 3D-printing process (Fig. 2b). An approximate three order of magnitude decrease in viscosity was observed when the shear rate increased from 0.1 s^{-1} to 100 s^{-1}, followed by a rapid increase to roughly the initial value when the shear rate was adjusted back to 0.1 s^{-1}. This high elasticity is the driving force for the structural integrity of the printed features, which in turn, enables the printing of thick electrodes. To further characterize the viscoelastic effect, stress sweep step (SSS) tests were carried out on the two inks, as shown in Fig. 2c. The two inks exhibit solid-like behavior (storage/elastic modulus (G') > loss/viscous modulus (G")) under an oscillation strain up to 9.38 and 20.77, indicating that the ink components form tenuous 3D elastic networks [36]. These results indicate that both inks exhibit the appropriate viscosity and thixotropic properties required for 3D printing.

To analyze the architecture of the electrodes, scanning electron microscopy (SEM) images of the rGO-AgNWs-LTO and rGO-LTO electrodes were taken after lyophilization and reduction. From the top-down images, it is observed that the hierarchical 3D architecture is constructed from continuous filaments with diameter (D) ~ 250 μm and interval (L) between two filaments ~500 μm. In addition to the macropores formed by the intersection of the fine filaments, additional micrometer-sized pores were produced on the surface of the filaments as a result of the freeze-drying procedure (Fig. 3a and Fig. S1a). An enlarged image reveals that the aperture of the micrometer-sized pores ranges

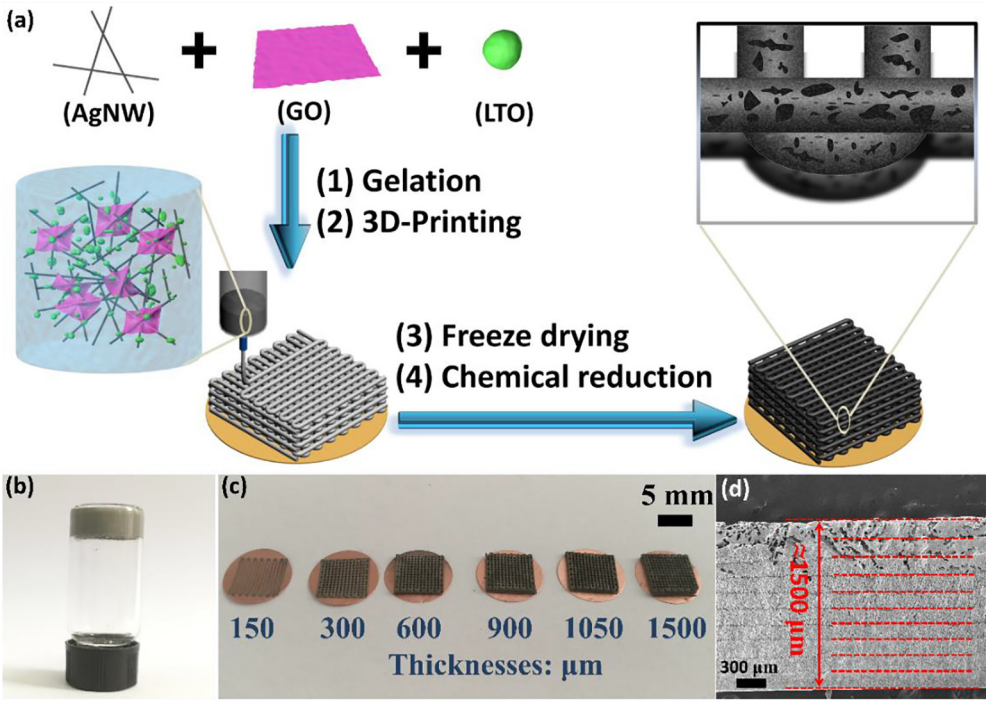

Fig. 1. (a) Schematic illustration of the fabrication process of the proposed 3D-printed architectures. (b) Optical photograph of the GO-AgNWs-LTO ink. (c) Digital image of 3D-printed rGO-AgNWs-LTO electrodes of different thicknesses after lyophilization. (d) Lateral view of an SEM image of the printed architectures, in which 3D-printed filaments are observed to be closely stacked closely with good layer-to-layer uniformity.

from several to tens of microns (Fig. 3b and Fig. S1b). These micrometer-sized pores in conjunction with the open mesh structure facilitate the penetration of the liquid electrolyte into the inner active sites, and act as a chamber to locally store the electrolyte [9,14,15]. From the cross-sectional images (Fig. 3c,d and Fig. S1c and d), it is seen that the LTO nanoparticles tightly adhere to the continuous 3D network. This continuous and conductive network facilitates the collection and transportation of electrons through the system [9,14,15]. Elemental mapping images verify that the LTO nanoparticles are homogenously dispersed in the AgNW-rGO network (Fig. 3e–h and Fig. S1e-g). In efforts to further characterize the pore structure of the rGO-AgNWs-LTO and rGO-LTO electrodes, full nitrogen sorption isotherms are shown in Fig. S2. Owning to nitrogen sorption isotherms can not measure micrometer-sized pores, it just exhibits type IV characteristics with a clear H3 hysteresis loop and indicates mesoporous characteristics [37]. The specific surface area and pore volume of rGO-AgNWs-LTO are 336.6 $m^2 g^{-1}$ and 0.14 $cm^3 g^{-1}$, respectively, which are much higher than those of rGO-LTO (101 $m^2 g^{-1}$ and 0.04 $cm^3 g^{-1}$). This is because the introduction of silver nanowires reduces the mutual stacking of rGO sheets to create more mesoporous structures.

The conductivity of the electrodes is a critical parameter regarding electrochemical performance. To analyze conductivity, four-point probe measurements were conducted on the two different electrodes following reduction. The conductivity of the functional rGO-AgNWs-LTO electrodes was measured to be approximately three orders of magnitude higher than that of the pure rGO-LTO electrodes (~1740 S cm^{-1}, and ~1.4 S cm^{-1} respectively) due to the introduction of the one-dimensional AgNWs (Fig. 3i).

The crystalline structure of the 3D architecture was investigated by XRD. The diffraction peaks of both architectures seen in Fig. 3j are indexed to pure LTO (JCPDS NO.49-0207). The diffraction peak located at 25.5° is attributed to the (0 0 2) plane of rGO, and indicates a good reduction of GO into rGO by the hydrazine hydrate vapor [38]. With the exception of silver nanowire and LTO peaks, no other impurity peaks are observed in either electrodes, indicating that the high-temperature hydrazine hydrate vapor used for reducing GO does not impact the crystalline nature of silver nanowires and LTO. The structural information of the 3D-printed architectures was further analyzed by Raman spectroscopy, as illustrated in Fig. 3k. The peaks located at 1348 and 1583 cm^{-1} are attributed to the D and G bands of graphene, respectively [38]. When comparing the intensity ratio between the two bands, the ratio I_D/I_G of rGO exceeds that of GO, suggesting a higher graphitization degree of rGO during the reduction procedure. This high degree of graphitization is beneficial in improving the mechanical properties of the electrode [34]. To quantify this mechanical performance, the printed rGO-AgNWs-LTO electrodes have a Young's

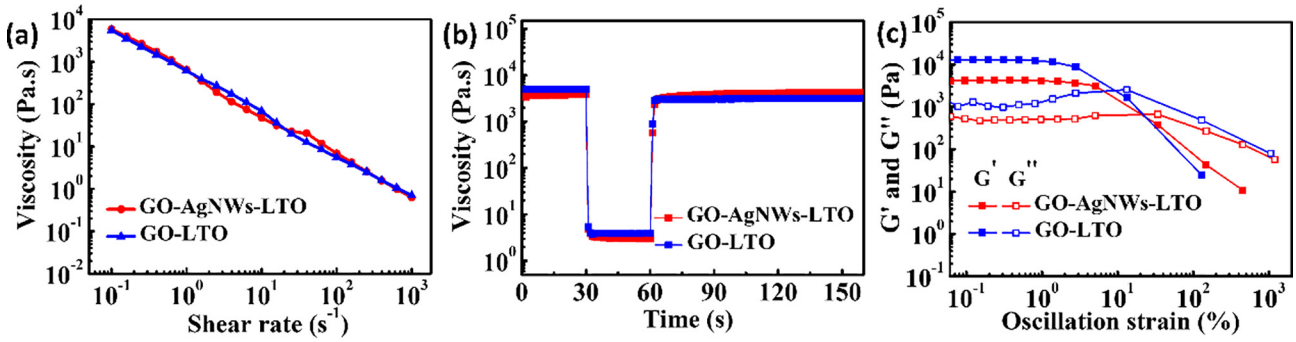

Fig. 2. (a) Viscosity as a function of shear rate for two inks. (b) Rheological behavior of the two inks during the extrusion printing process. (c) Storage (G') and loss (G") moduli as a function of oscillation strain for two inks.

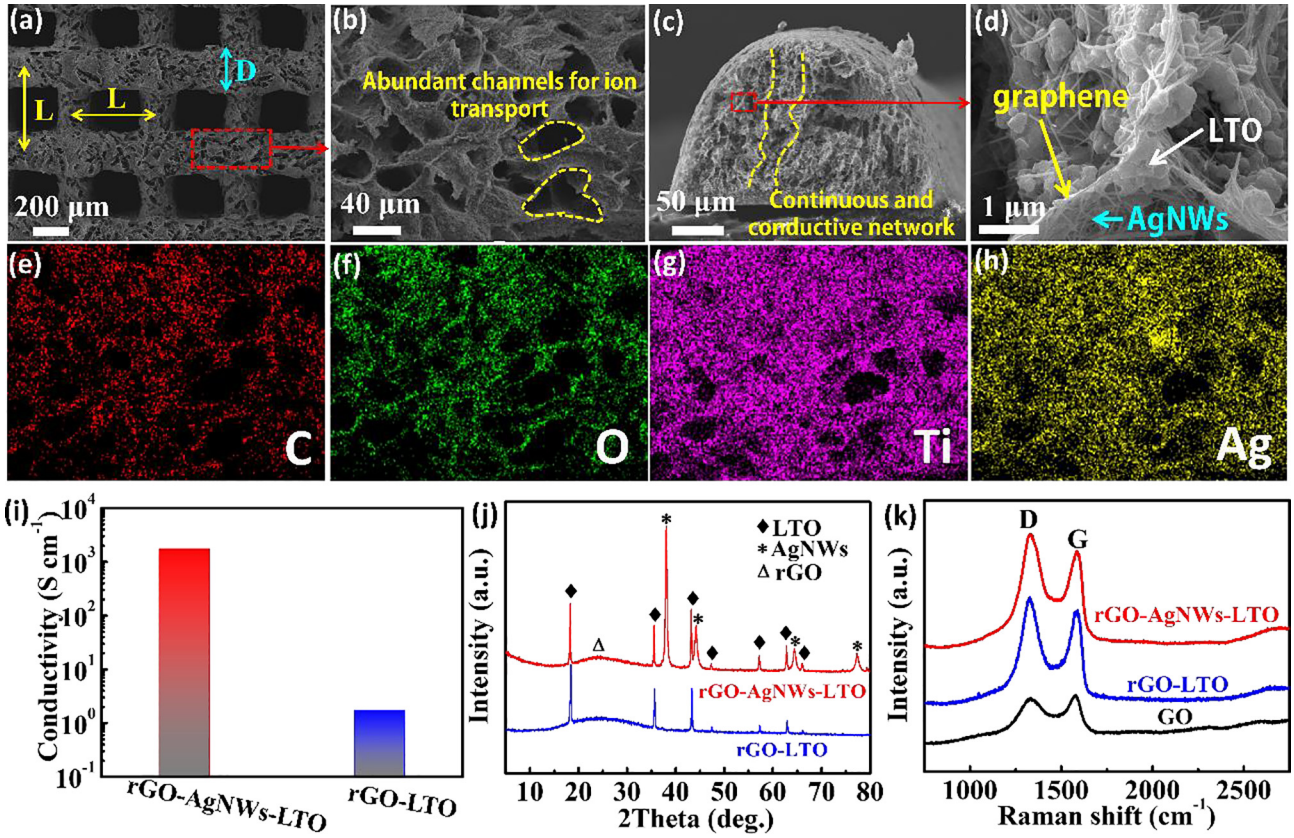

Fig. 3. (a) Top-down SEM image and (b) magnified top-down SEM image of the 3D-printed rGO-AgNWs-LTO electrode. (c) Cross-sectional SEM image and (d) magnified cross sectional SEM image of the 3D-printed rGO-AgNWs-LTO electrodes. Elemental mapping images of (e) C; (f) O; (g) Ti; and (h) Ag species for the 3D-printed rGO-AgNWs-LTO electrodes. (i) Electrical conductivity; (j) XRD patterns; and (k) Raman pattern of the 3D-printed rGO-AgNWs-LTO and rGO-LTO electrodes.

modulus of 361.66 KPa, sufficient to enable the battery to circulate during the charging and discharging process (Fig. S3).

Following electrical characterization, the electrochemical performance of the 3D-printed rGO-AgNWs-LTO and rGO-LTO electrodes of 150 μm thickness was investigated via cyclic voltammetry (CV). Using this method, the LTO based electrodes were placed on top of a polypropylene separator (Celgard 2300), with lithium metal used as both the counter and reference electrode. A liquid electrolyte (1 M $LiPF_6$ in a mixture of ethylene carbonate (EC), diethyl carbonate (DEC), and dimethyl carbonate (DMC) with a volume ratio of 1:1:1) was subsequently injected into the cell. Fig. 4a shows the CV profiles of both electrodes at a scan rate of 0.5 mV s^{-1} in a voltage window of 1.0–2.5 V (vs. Li/Li^+). Well-defined redox peaks at 1.721/1.459 V and 1.835/1.323 V were observed for rGO-AgNWs-LTO and rGO-LTO electrodes, respectively, which are characteristic of a Ti^{4+}/Ti^{3+} redox couple reaction. The presence of these peaks reflects the Li-ion extraction and insertion into the LTO [22,38]. Furthermore, the symmetry of the redox peaks suggests excellent reversibility of these electrodes. It is observed that the redox peaks of the rGO-AgNWs-LTO electrode are sharper, and less polarized than those of the rGO-LTO electrodes, indicating that the rGO-AgNWs-LTO electrode has faster reaction kinetics.

To further evaluate the electrochemical performance of the electrodes with regards to lithium storage, galvanostatic charge-discharge measurements were conducted at rates ranging from 0.5 to 10C (1C = 175 mAh g^{-1}). The charge–discharge curves of the 150 μm thickness electrodes obtained between 1.0 and 2.5 V (vs. Li/Li^+) at C-rates of 0.5–10C are presented in Fig. 4b and c. The discharge curves for the rGO-AgNWs-LTO electrodes remain flat plateaus which were the typical discharge behavior of spinel LTO, as observed from a dominant plateau of 1.55 V of all rates. In contrast, the potential plateaus of the reference rGO-LTO electrodes become shorter and gradually bend as the C-rate increases. This behavior also indicates that the rGO-AgNWs-LTO electrodes have a lower polarization, which can be attributed to the improvement of electrical conductivity with the introduction of the AgNWs into the ink. Fig. 4d compares the rate performance of 150 μm thick rGO-AgNWs-LTO and rGO-LTO electrodes at C-rates of 0.5–10C. When the current density increases from 0.5 to 1, 2, 5, and 10C, the rGO-AgNWs-LTO electrode deliver a specific capacity of 177.5, 169.7, 161.5, 142.9 and 121 mAh g^{-1}, respectively. However, the rGO-LTO electrodes just deliver a specific capacity of 192.2, 168.4, 132.2, 79 and 19.4 mAh g^{-1} at the current densities of 0.5, 1, 2, 5 and 10C. As a note, the specific capacities of the rGO-LTO electrode is slightly higher than its rGO-AgNWs-LTO counterpart at 0.5C as the rGO-LTO electrodes have a greater concentration of rGO, which contributes to the overall capacity value. It is evident that the rGO-AgNWs-LTO electrodes exhibit much better rate performance than that of the rGO-LTO electrode. Then, the rate performance of rGO-AgNWs-LTO electrodes with different thicknesses was tested (Fig. S4). When the thickness of rGO-AgNWs-LTO electrodes increases from 300 to 900 μm, the rate performance decreases obviously at the current density of 5C. However, rGO-AgNWs-LTO electrodes with 300, 600, 900 μm thickness can still deliver a specific capacity of 148.8, 141.9 and 132.8 mAh g^{-1} at the current densities of 2C. These values exceed those of most reported 3D-printed LTO/carbon electrodes to date [17,19,39,40].

The cycle performance of the electrodes at 5C-rate is illustrated in Fig. 4e. The activation process in the first three cycles has a decrease in capacity due to the generation of solid-electrolyte interphases (SEI). It can be observed from the figure that the capacity value is retained at 91% and 33% of the fourth discharge capacity after 200 cycles for the two electrodes. From the charge-discharge curves in Fig. S5, it can be further deduced that the discharge curves of the rGO-AgNWs-LTO electrodes are somewhat polarized (compared to low current density),

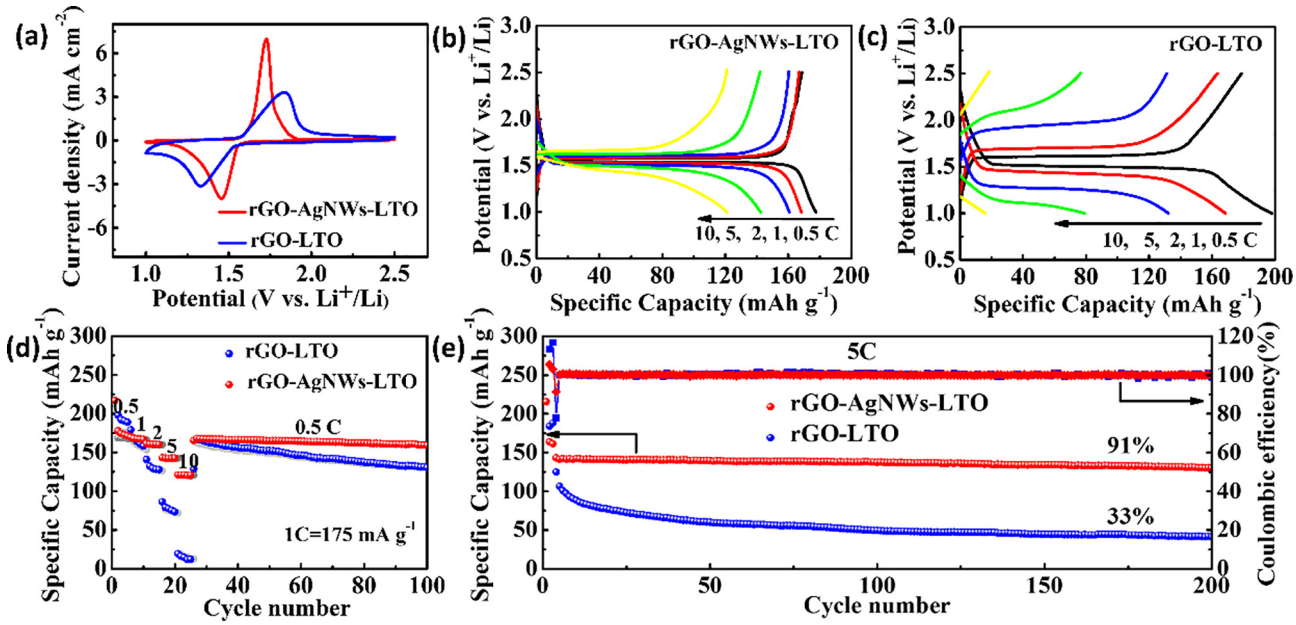

Fig. 4. Electrochemical performance of the 3D-printed electrodes with a thickness of 150 μm. (a) Cyclic voltammetry data for cells with rGO-AgNWs-LTO and rGO-LTO electrodes. (b) Charge-discharge voltage curves of 3D-printed rGO-AgNWs-LTO, and (c) rGO-LTO electrodes at different rates (0.5C, 1C, 2C, 5C, and 10C). (d) Rate performance comparison of 3D-printed rGO-AgNWs-LTO and rGO-LTO electrodes. (e) Capacity of 3D-printed rGO-AgNWs-LTO and rGO-LTO electrodes at 5C for 200 cycles. The first three cycles are activation process at 0.2C.

as the flatness of the platform is still stronger than that of the rGO-LTO electrodes. From the standpoint of both the cycle performance and the rate performance, the rGO-AgNWs-LTO electrodes exhibit better performance metrics than that of the rGO-LTO electrodes.

One primary advantage of 3D printing technology is the increase of thickness of electrodes afforded by the layer-by-layer printing process, which additionally reduces the ratio of electrochemically inactive components in stacked energy storage devices. The reduction of these inactive components further leads to improvements in areal capacity and manufacturing costs [9,13]. However, one drawback is the increased difficulty in transmission of ions and electrons with increasing electrode thickness. To study this phenomenon, AC impedance measurements were carried out to explore the effect of thickness variation on the kinetic process of the electrodes (Fig. 5a and b). Nyquist plots of the rGO-AgNWs-LTO electrodes are illustrated in Fig. 5a, with thicknesses of the electrode ranging from 150 μm to 1050 μm. Each of the plotted curves consists of a depressed semicircle at high frequencies, and a straight line at low frequencies. These features can be attributed to the charge transfer process at the electrolyte–electrode interface, and the Li-ion diffusion in the bulk of electrode, respectively [13]. As expected, the charge transfer resistance increases with increasing electrode thickness. However, the Li-ion diffusion resistance of all electrodes is effectively constant due to the interconnected channels providing convenient conditions for the infiltration of the electrolyte.

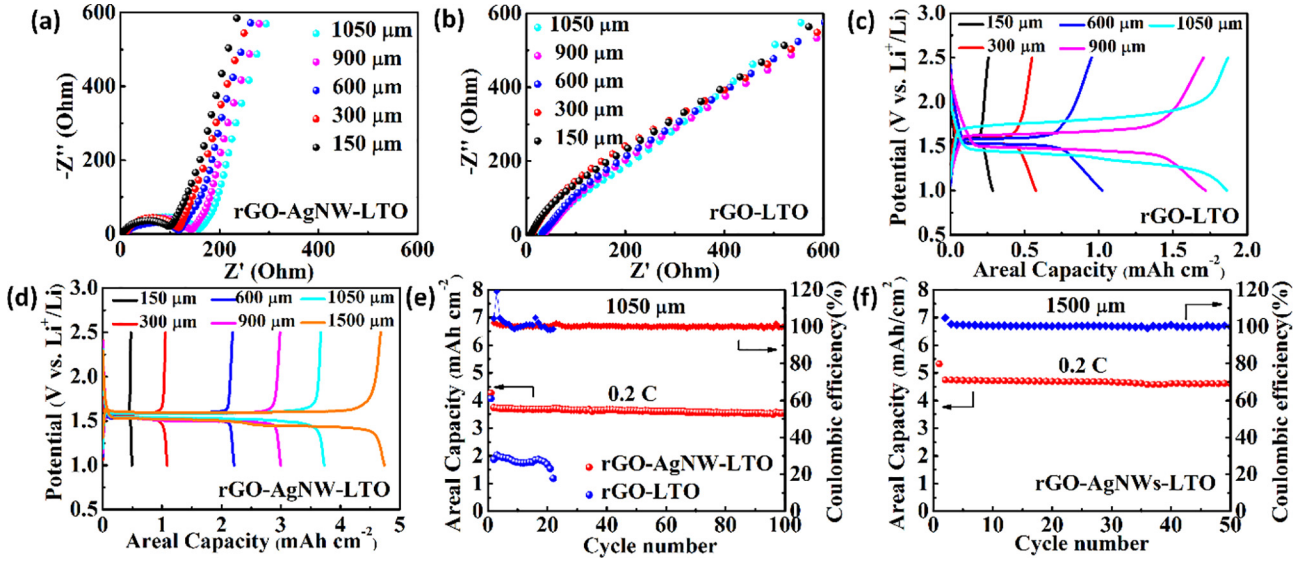

Fig. 5. (a) AC impedance measurements of cells for 3D-printed rGO-AgNWs-LTO electrodes of different thicknesses. (b) AC impedance measurements of cells for rGO-LTO electrodes of different thicknesses. (c) Charge-discharge voltage curves of different thick 3D-printed rGO-LTO electrodes of 3th at 0.2C. (d) Charge-discharge voltage curves of different thick 3D-printed rGO-AgNWs-LTO electrodes of 3th at 0.2C. (e) Areal capacity and Coulombic efficiency of 3D-printed rGO-AgNWs-LTO and rGO-LTO electrodes of 1050 μm thickness at 0.2C current density when cycled for 100 cycles. (f) High areal capacity and coulombic efficiency of 3D-printed rGO-AgNWs-LTO electrodes with 1500 μm thickness at current density of 0.2C (1.06 mA cm^{-2}) for 50 cycles.

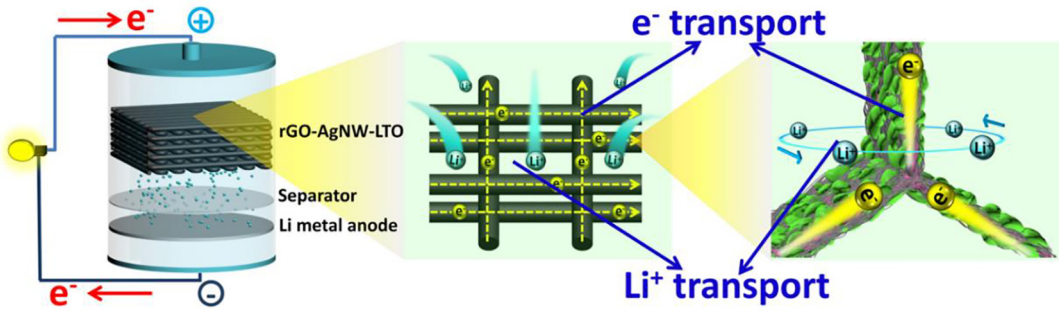

Fig. 6. Graphical illustrations of the ion and electron transportation behavior occurring in the 3D-printed rGO-AgNWs-LTO electrodes / separator / Li metal battery system, and the 3D-printed rGO-AgNWs-LTO electrodes during the discharging processes.

As a comparison, the Nyquist plots of rGO-LTO electrodes of different thicknesses were also measured, and illustrated in Fig. 5b. Due to the low conductivity of the electrodes, the charge transfer resistance was significantly higher than their rGO-AgNWs-LTO counterparts at the same thickness. As a note, the straight lines at low frequencies of rGO-AgNWs-LTO were obviously steeper than rGO-LTO which indicates that Li-ion diffuses faster in the former. This is because the introduction of silver nanowires reduces the mutual stacking of rGO sheets to create more microporous structures inside the electrodes. The BET results (Fig. S2 in the SI) also confirmed this point.

To assess the impact of thickness on cycling performance, galvanostatic cycling tests at a current density of 0.2C were carried out on the two types of electrodes with thicknesses ranging from 150 μm to 1500 μm (Fig. 5c and d). The areal capacity is observed to increase with increasing electrode thickness as expected, but the voltage platform of the rGO-AgNWs-LTO electrodes is more gradual than that of the rGO-LTO electrodes. Furthermore, the areal capacity is approximately twice that of the rGO-LTO electrodes at the same thickness. Cycling performance of rGO-AgNWs-LTO electrodes with thicknesses ranging from 150 μm to 900 μm at a current density of 1C also show better cyclic stability than rGO-LTO electrodes (Fig. S6). The areal capacity of the rGO-AgNWs-LTO electrodes with 1500 μm thickness can still reach up to 4.74 mAh cm^{-2} at the third cycle (with a high active material mass loading of ~30 mg cm^{-2}). In contrast, the voltage platform of 1050 μm thick rGO-LTO electrode shows a distinct downward trend. This behavior suggests that this thickness is the upper limit for the thickness of 3D-printed rGO-LTO electrodes.

The cycling performance of the two electrodes was conducted and compared at the maximum thickness of 1050 μm at a current density of 0.2C. Fig. 5e illustrates a stable areal capacity of the rGO-AgNWs-LTO electrode of ~3.55 mAh cm^{-2} after 100 cycles, representing a capacity retention 95%. In contrast, the rGO-LTO electrodes was only able to maintain 20 cycles at an areal capacity of ~1.1 mAh cm^{-2}. Because the conductivity of rGO is not high enough to maintain the smooth transmission of electrons. This will lead to separator deformation and short circuit of the battery due to the rapid heat release inside the battery. We dismantled the battery with rGO-LTO after 20 cycles and found that the separator had melted and deformed (Fig. S7b). To further quantify the potential of the thick rGO-AgNWs-LTO electrodes with regards to electrochemical performance, the cycling performance of 1500 μm thick 3D-printed rGO-AgNWs-LTO electrodes was measured at a current density of 0.2C. A stable areal capacity of ~ 4.61 mAh cm^{-2} after 50 cycles is illustrated in Fig. 5f, representing a capacity retention of 97.2%. 3D-printed rGO-AgNWs-LTO electrode with 1500 μm can still show 31.60 mAh cm^{-3} vol capacity (Fig. S8). These metrics of capacity and cycling performance are comparable to, or exceed those of certain Si and metal oxide based devices, even though the gravimetric specific capacity of LTO is lower than that of Si and metal oxides [23–31], and are significant for the investigation and development of high-performance LIBs.

These advanced electrochemical performance metrics can be attributed to the unique architectural design and material selection used in the rGO-AgNWs-LTO electrode. An illustration of how these electrodes improve the charge and ion transfer kinetics is presented in Fig. 6. Firstly, the open mesh structure (~250 μm wide square pores) and abundant micropores on the filament surface facilitates penetration of the liquid electrolyte into inner active sites, and acts as a chamber to locally store the electrolyte. This action ensures a stable electrochemical environment for Li-ion transfer in the charging and discharging process. Secondly, the 3D conductive network formed by the AgNWs tightly enclose the LTO nanoparticles and facilitate the rapid transmission of electrons from the inside to the edge, even in extremely thick electrodes. Finally, the graphene network provides the required mechanical strength and toughness, which is conducive to improving the stability of the electrodes. As a result of the synergistic contributions of all materials, the thickness of the electrode can be increased, which greatly improves both the areal capacity and the rate-performance.

4. Conclusion

In this work, the design and fabrication of 3D porous, highly conductive, and thick electrodes were presented. These electrodes were fabricated through a facile extrusion-based 3D printing process of a viscous gel-like nanocomposite ink comprising AgNWs, GO nanosheets and LTO nanoparticles. By optimizing the printing process and the raw materials, ultra-thick electrodes (thickness of ~1500 μm) can be effectively fabricated. Batteries utilizing these 3D electrodes exhibit a highly improved rate capability (discharge 121 mAh g^{-1} at 10C), and high areal capacity (4.74 mAh cm^{-2} at a current density of 1.06 mA cm^{-2}). This areal capacity is comparable to, or exceeds some reported areal capacities of Si and metal oxide based devices, even though the gravimetric specific capacity of LTO is lower than that of Si and metal oxides [23–31]. The mechanical strength and conductivity of the electrodes also ensure that the electrochemical performance is robust, with the electrodes retaining 95.5% of their original capacity after 100 cycles. This work thus provides an avenue to achieving thick electrodes by mitigating the issues of partial electrolyte infiltration, poor mechanical performance, and slow charge transport. Furthermore, the design of these thick electrodes may be easily translated and applied to other energy storage devices.

Acknowledgements

The work reported here was supported by NSFC (51872146, 51633002, 91633301, 21421001), Tianjin Municipal Science and Technology Commission (17JCZDJC30200) in China, and MoST (2016YFA0200200).

Appendix A. Supplementary data

Supplementary data to this article can be found online at https://doi.org/10.1016/j.cej.2019.122641.

References

[1] J.M. Tarascon, M. Armand, Issues and challenges facing rechargeable lithium batteries, Nature 171–179 (2011).
[2] J.B. Goodenough, K.S. Park, The Li-ion rechargeable battery: a perspective, J. Am. Chem. Soc. 135 (2013) 1167–1176.
[3] L.X. Yuan, Z.H. Wang, W.X. Zhang, X.L. Hu, J.T. Chen, Y.H. Huang, J.B. Goodenough, Development and challenges of $LiFePO_4$ cathode material for lithium-ion batteries, Energy Environ. Sci. 4 (2011) 269–284.
[4] Q.N. Zhao, K.Q. Zhao, G.P. Ji, X.L. Guo, M. Han, J. Wen, Z.L. Ren, S.C. Gao, R.H. Wang, M. Li, K. Sun, N. Hu, C.H. Xu, High sulfur loading, rGO-linked and polymer binder-free cathodes based on rGO wrapped N, P-codoped mesoporous carbon as sulfur host for Li-S batteries, Chem Eng. J. 361 (2019) 1043–1052.
[5] S.H. Lee, Y.R. Jo, Y. Noh, B.J. Kim, W.B. Kim, Fabrication of hierarchically branched SnO2 nanowires by two-step deposition method and their applications to electrocatalyst support and Li ion electrode, J. Power Sources 367 (2017) 1–7.
[6] X.M. Ma, Z.P. Wei, H.J. Han, X.B. Wang, K.Q. Cui, L. Yang, Tunable construction of multi-shell hollow SiO_2 microspheres with hierarchically porous structure as high-performance anodes for lithium-ion batteries, Chem. Eng. J. 323 (2017) 252–259.
[7] S.H. Lee, Y. Noh, W.B. Kim, Convex and concave square arrays of vertical SnO_2 nanowire bundles toward lithium-ion storage electrodes, Energy Technol. 5 (2017) 1507–1513.
[8] L.B. Hu, F.L. Mantia, H. Wu, X. Xie, J. McDonough, M. Pasta, Y. Cui, Lithium-ion textile batteries with large areal mass loading, Adv. Energy Mater. 1 (2011) 1012–1017.
[9] C.J. Chen, Y. Zhang, Y.J. Li, Y.D. Kuang, J.W. Song, W. Luo, Y.B. Wang, Y.G. Yao, G. Pastel, J. Xie, L.B. Hu, Highly conductive, lightweight, low-tortuosity carbon frameworks as ultrathick 3D current collectors, Adv. Energy Mater. 7 (2017) 1700595.
[10] W. Lai, C.K. Erdonmez, T.F. Marinis, C.K. Bjune, N.J. Dudney, F. Xu, R. Wartena, Y.M. Chiang, Ultrahigh-energy-density microbatteries enabled by new electrode architecture and micropackaging design, Adv. Mater. 22 (2010) E139–E144.
[11] J.H. Prosser, T. Brugarolas, S. Lee, A.J. Nolte, D. Lee, Avoiding cracks in nanoparticle films, Nano Lett. 12 (2012) 5287–5291.
[12] D. Lv, J. Zheng, Q. Li, X. Xie, S. Ferrara, Z. Nie, L.B. Mehdi, N.D. Browning, J.G. Zhang, G.L. Graff, J. Liu, J. Xiao, High energy density lithium-sulfur batteries: Challenges of thick sulfur cathodes, Adv. Energy Mater. 5 (2015) 1402290.
[13] T.S. Wei, B.Y. Ahn, J. Grotto, J.A. Lewis, 3D Printing of customized Li-Ion batteries with thick electrodes, Adv. Mater. 30 (2018) 1703027.
[14] J.S. Sander, R.M. Erb, L. Li, A. Gurijala, Y.M. Chiang, High-performance battery electrodes via magnetic templating, Nat. Energy. 1 (2016) 16099.
[15] Y.D. Kuang, C.J. Chen, G. Pastel, Y.J. Li, J.W. Song, R.Y. Mi, W.Q. Kong, B.Y. Liu, Y.Q. Jiang, K. Yang, L.B. Hu, Conductive cellulose nanofber enabled thick electrode for compact and flexible energy storage devices, Adv. Energy Mater. 8 (2018) 1802398.
[16] E.C. Self, R. Wycisk, P.N. Pintauro, Electrospun titania-based fibers for high areal capacity Li-ion battery anodes, J. Power Sources. 282 (2015) 187–193.
[17] K. Sun, T.S. Wei, B.Y. Ahn, J.Y. Seo, S.J. Dillon, J.A. Lewis, 3D printing of interdigitated Li-Ion microbattery architectures, Adv. Mater. 25 (2013) 4539–4543.
[18] K. Fu, Y.G. Yao, J. Dai, L.B. Hu, Progress in 3D printing of carbon materials for energy-related applications, Adv. Mater. 29 (2017) 1603486.
[19] K. Fu, Y.B. Wang, C.Y. Yan, Y.G. Yao, Y.N. Chen, J.Q. Dai, S. Lacey, Y.B. Wang, J.Y. Wan, T. Li, Z.G. Wang, Y. Xu, L.B. Hu, Graphene oxide-based electrode inks for 3D-printed lithium-ion batteries, Adv. Mater. 28 (2016) 2587–2594.
[20] J.W. Ding, K. Shen, Z.G. Du, B. Li, S.B. Yang, 3D-printed hierarchical porous frameworks for sodium storage, ACS. Appl. Mater. Interfaces. 9 (2017) 41871–41877.
[21] K. Shen, H.L. Mei, B. Li, J.W. Ding, S.B. Yang, 3D printing sulfur copolymer-graphene architectures for Li-S batteries, Adv. Energy Mater. 8 (2018) 1701527.
[22] Y.X. Zhu, J.X. Qiu, Y.Q. Huang, P. Wang, C. Lai, Enhanced cycling performance of the $Li_4Ti_5O_{12}$ anode in an ethers electrolyte induced by a solid-electrolyte interphase film, RSC Adv. 5 (2015) 56908–56912.
[23] X.M. Xu, P.J. Wu, Q. Li, W. Yang, X. Zhang, X.P. Wang, J.S. Meng, C.J. Niu, L.Q. Mai, Realizing stable lithium and sodium storage with high areal capacity using novel nanosheetassembled compact CaV4O9 microflowers, Nano Energy. (2018), https://doi.org/10.1016/j.nanoen.2018.06.012.
[24] X.H. Wang, Y. Fan, R.A. Susantyoko, Q.Z. Xiao, L.M. Sun, D.Y. He, Q. Zhang, High areal capacity Li ion battery anode based on thick mesoporous Co_3O_4 nanosheet networks, Nano Energy. 5 (2014) 91–96.
[25] C. Han, X. Zhang, X.M. Xu, Q. He, J.S. Meng, X.P. Wang, Z. Liu, P.J. Wu, L.Q. Mai, Porous $CaFe_2O_4$ as a promising lithium ion battery anode: a trade-off between high capacity and long-term stability, Nanoscale 10 (2018) 12963–12969.
[26] N. Liu, Z. Lu, J. Zhao, M.T. McDowell, H.W. Lee, W.T. Zhao, Y. Cui, A pomegranate-inspired nanoscale design for large-volume-change lithium battery anodes, Nature Nanotech. 9 (2014) 187.
[27] H.J. Tian, X.J. Tan, F.X. Xin, C.S. Wang, W.Q. Han, Micro-sized nano-porous Si/C anodes for lithium ion batteries, Nano Energy. 11 (2015) 490–499.
[28] D.C. Lin, Z.D. Lu, P.C. Hsu, H.R. Lee, N. Liu, J. Zhao, H.T. Wang, C. Liu, Y. Cui, A high tap density secondary silicon particle anode fabricated by scalable mechanical pressing for lithium-ion batteries, Energy Environ. Sci. 8 (2015) 2371–2376.
[29] X.H. Wang, L.M. Sun, R.A. Susantyoko, Q. Zhang, A hierarchical 3D carbon nanostructure for high areal capacity and flexible lithium ion batteries, Carbon 98 (2016) 504–509.
[30] Q. Xu, J.Y. Li, J.K. Sun, Y.X. Yin, L.J. Wan, Y.G. Guo, Watermelon-inspired Si/C microspheres with hierarchical buffer structures for densely compacted lithium-ion battery anodes, Adv. Energy Mater. 7 (2017) 1601481.
[31] Q.B. Zhang, H.X. Chen, L.L. Luo, B. Zhao, H. Luo, X. Han, J.W. Wang, C.M. Wang, Y. Yang, T. Zhu, M.L. Liu, Harnessing the concurrent reaction dynamics in active Si and Ge to achieve high performance lithium-ion batteries, Energy Environ. Sci. 11 (2018) 669–681.
[32] S.R. Liu, J.P. Li, X.L. Shi, E.L. Gao, Z.P. Xu, H.H. Tang, K. Tong, Q.B. Pei, J.J. Liang, Y.S. Chen, Rollerball-pen-drawing technology for extremely foldable paper-based electronics, Adv. Electron. Mater. 3 (2017) 1700098.
[33] X.L. Shi, S.R. Liu, Y. Yang, J.J. Liang, Y.S. Chen, Lowering internal friction of 0D–1D-2D ternary nanocomposite-based strain sensor by fullerene to boost the sensing performance, Adv. Funct. Mater. 28 (2018) 1800850.
[34] P. Xue, S.R. Liu, X.L. Shi, C. Sun, C. Lai, Y. Zhou, D. Sui, Y.S. Chen, J.J. Lang, A hierarchical silver-nanowire-graphene host enabling ultrahigh rates and superior long-term cycling of lithium-metal composite anodes, Adv. Mater. 30 (2018) 1804165.
[35] S.R. Liu, X.L. Shi, X.R. Li, Y. Sun, J. Zhu, Q.B. Pei, J.J. Lang, Y.S. Chen, A general gelation strategy for 1D nanowires: dynamically stable functional gels for 3D printing flexible electronics, Nanoscale 10 (2018) 20096–20107.
[36] S.H. Kim, K.H. Choi, S.J. Cho, S. Choi, S. Park, S.Y. Lee, Printable solid-state lithium-ion batteries: a new route toward shape-conformable power sources with aesthetic versatility for flexible electronics, Nano Lett. 15 (2015) 5168–5177.
[37] Y. Wang, H. Dou, J. Wang, B. Ding, Y.L. Xu, Z. Chang, X.D. Hao, Three-dimensional porous MXene/layered double hydroxide composite for high performance supercapacitors, J. Power Sources 327 (2016) 221–228.
[38] S.D. Lacey, D.J. Kirsch, Y.J. Li, J.T. Morgenstern, B.C. Zarket, Y.G. Yao, J.Q. Dai, L.Q. Garcia, B.Y. Liu, T.T. Gao, S.M. Xu, S.R. Raghavan, J.W. Connell, Y. Lin, L.B. Hu, Extrusion-based 3D printing of hierarchically porous advanced battery electrodes, Adv. Mater. 30 (2018) 1705651.
[39] R.R. Kohlmeyer, A.J. Blake, J.O. Hardin, E.A. Carmona, J. C-Nunez, B.J. Maruyama, J.D. Berrigan, H. Huang, M.F. Durstock, Composite batteries: a simple yet universal approach to 3D printable lithium-ion battery electrodes, J. Mater. Chem. A. 4 (2016) 16856–16864.
[40] Y.B. Wang, C.J. Chen, H. Xie, T.T. Gao, Y.G. Yao, G. Pastel, X.G. Han, Y.J. Li, J.P. Zhao, K. Fu, L.B. Hu, 3D-printed all-fiber li-ion battery toward wearable energy storage, Adv. Funct. Mater. 27 (2017) 1703140.